Research Square

Preprints are preliminary reports that have not undergone peer review.
They should not be considered conclusive, used to inform clinical practice,
or referenced by the media as validated information.

Micro/Nanoplastic Formation by Polymer Processing

Sanat Kumar

sk2794@columbia.edu

Columbia University https://orcid.org/0000-0002-6690-2221

Shrishti Das

columbia university https://orcid.org/0009-0003-9555-3360

Javed Akhtar

Indian Institute of Technology-Madras

Aaron Burkey

National Institute of Standards and Technology

Aihika Mandal

Indian Institute of Technology-Bombay

Guruswamy Kumaraswamy

IIT

Tarak Patra

Indian Institute of Technology https://orcid.org/0000-0002-6002-0922

Physical Sciences - Article

Keywords:

Posted Date: August 10th, 2026

DOI: https://doi.org/10.21203/rs.3.rs-10579684/v1

License: This work is licensed under a Creative Commons Attribution 4.0 International License.
Read Full License

Additional Declarations: There is **NO** Competing Interest.

Micro/Nanoplastic Formation by Polymer Processing

Shrishti Das[1], Javed Akhtar[2], Aaron Burkey[3], Aihika Mandal[4], Guruswamy Kumaraswamy[4], Tarak K. Patra[2], and Sanat K. Kumar[1,*]

[1]*Department of Chemical Engineering, Columbia University, New York, New York 10027*

[2]*Department of Chemical Engineering, Indian Institute of Technology, Madras, Chennai 600036, India*

[3]*National Institute of Standards and Technology, Materials Science and Engineering Division, MD 20899*

[4]*Department of Chemical Engineering, Indian Institute of Technology, Bombay 400076, India*

Micro and nanoplastics (MNPL) are widely recognized to form when solid-state polymers are exposed to external cues (e.g., stress, UV, oxygen) (1–7). While melt extrusion, a routine step in polymer manufacturing and recycling, is generally not considered a source of MNPL, we combine experiments, molecular dynamics (MD) simulations and extensive materials characterization to show that it generates substantial quantities of MNPL, even under industrially relevant processing conditions. The effect is general, occurring across six polymer chemistries—polypropylene, two polyethylenes, polystyrene, nylon and polycarbonate—spanning semicrystalline and amorphous morphologies that together account for most plastics produced. The underlying physics is the enthalpic penalty for mixing short oxidized chains, formed during extrusion, with the native polymer, leading to phase separated inclusions. The resulting weak interfacial adhesion between coexisting phases promotes embrittlement and MNPL release. In semicrystalline polymers, post-extrusion crystallization further exacerbates this effect by selectively transporting short oxidized chains to interfaces, like the air–polymer boundary, despite their high surface energy. Our results identify polymer processing as an intrinsic source of plastic pollution and indicates that mitigation will require strategies that suppress or heal chain scission at the source.

Microplastics (< 5 mm) and nanoplastics (< 1 μm) (8) are of concern due to their environmental persistence and biological impact (9). MNPL possess high specific surface area, enabling them to adsorb metals, pollutants and microorganisms (10). Their small sizes facilitates their ready entry into living organisms, (3, 11–14) causing a wide range of disorders (13, 15–17). Thus, identifying the sources of MNPL and elucidating the mechanisms governing their formation and mitigation remain critical challenges.

It is well-recognized that MNPL can be created during several stages of a polymer's life cycle. During routine polymer use, they can be generated by both intrinsic [e.g., thermal and/or mechanical stresses (4)] and extrinsic factors [e.g., oxidation (6, 7, 18–20), UV radiation (7), mechanical abrasion (5, 21–23)]. Extrinsic conditions facilitate chemi-crystallization, void formation, cracking, and embrittlement, which lead to polymer fragmentation into MNPL (1, 24). Post-use, MNPL are created during polymer reprocessing [e.g., shredding during mechanical recycling (25)], or during end-of-life management, including landfilling (26) and incineration (27). In contrast to these established pathways for MNPL formation from solid-state polymers, we demonstrate that the routine melt processing of both semicrystalline and amorphous polymers can generate MNPL. Specifically, we show, in agreement with established knowledge, that extrusion induces chain scission, generating short oxygenated chains. MD simulations and complementary experiments then illustrate that these short functionalized chains enthalpically dislike the bulk polymer matrix, driving phase separation, embrittlement, and MNPL release.

We demonstrate this phenomenon in detail on isotactic polypropylene (PP) and polyethylene (PE, including high density PE, HDPE, and linear low density PE, LLDPE), representative of the class of non-polar semicrystalline polymers. The MNPL produced were characterized by a suite of techniques: scanning electron microscopy (SEM), light scattering, attenuated total reflection Fourier transform infrared spectroscopy (ATR-FTIR), nuclear magnetic resonance (NMR), thermogravimetric analysis (TGA), differential scanning calorimetry (DSC), high-temperature size-exclusion chromatography (HT-SEC), and small/wide-angle X-ray scattering (SAXS/WAXS). To support these studies we show that glassy amorphous non-polar polystyrene (PS) also generates MNPL. Finally, to establish generality, we verify that two oxygen containing polymers, nylon-6 (semicrystalline) and bisphenol-A-polycarbonate (amorphous) also behave similarly.

A New Pathway of MNPL Creation During Routine Processing: PP was extruded under conditions representative of industrial practice, using short residence times ($\approx$ 5 min) (Figures 1A, S1, S2). Irrespective of the extrusion speed chosen (21 rad/s, 26 rad/s, 31 rad/s), when the extruded polymer was quenched to room temperature and subsequently brought into contact with HPLC water, the supernatant exhibited higher light scattering count rates relative to when water was added to virgin, unextruded polymer (Figures 1A, S2). (Pure water by itself also results in scattering that is comparable to the last control.) This suggests the formation of a greater number of dispersed particles from the extruded samples. It is important to note that the light scattering intensity convolves the MNPL concentration, size and shape, making it difficult to unambiguously determine the MNPL size or concentration from the scattering intensity. Instead (1), the scattering intensity is used as a proxy that convolves these factors.

Evaporation of the water, followed by vacuum drying at 40 °C for 12 h, yielded a white powder ($\approx$ 0.2 wt% of total polymer mass), consisting of MNPL (Figures 1B, S1, S3). Electron microscopy results show that the

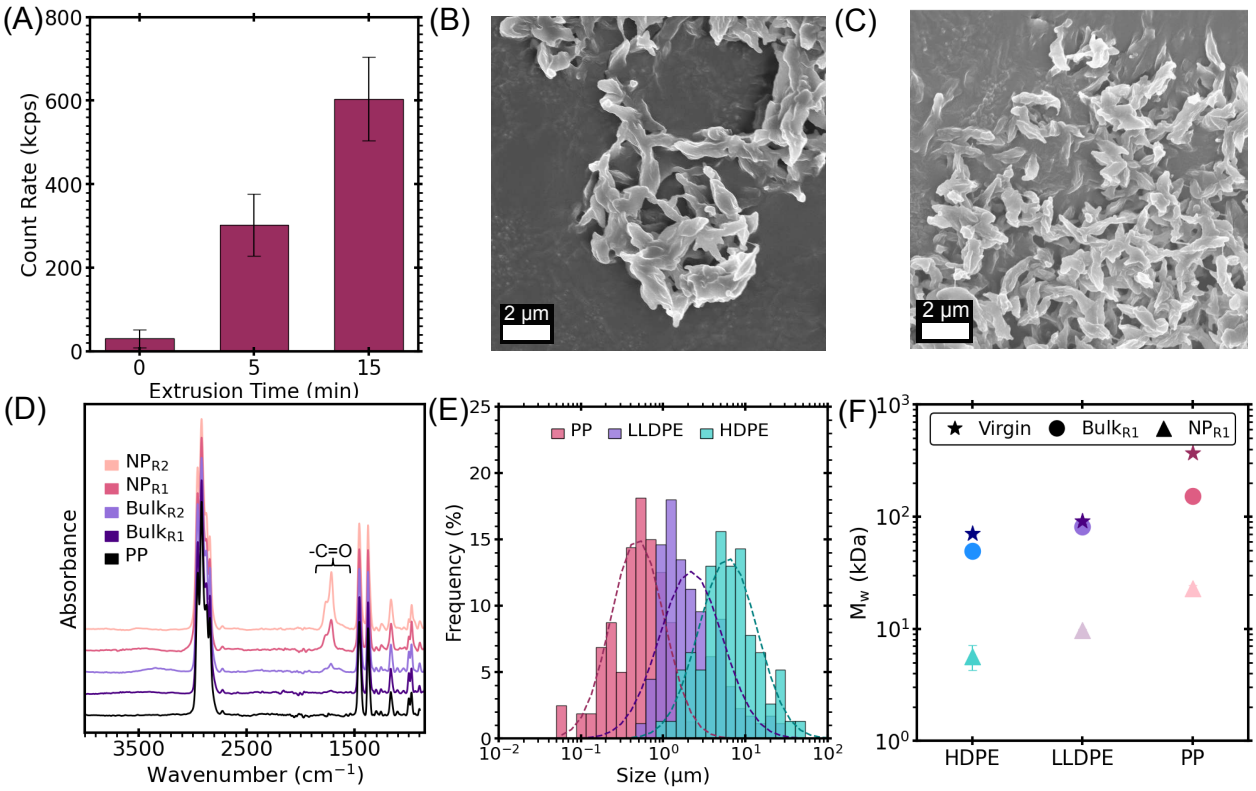


Figure 1: **MNPL Release Through Polymer Melt Extrusion.** (A) Light scattering count rates of the supernatant water collected from virgin polymer (control, shown as 0 min), and after extrusion for 5 min and 15 min at 21 rad/s. SEM micrographs of white powder collected after the extrusion of PP for (B) 5 min and (C) 15 min. (D) ATR-FTIR absorbance spectra of virgin PP (labeled PP), bulk PP after the first ($Bulk_{R1}$) and second extrusion ($Bulk_{R2}$), along with MNPL collected after the first (NP_{R1}) and second extrusion (NP_{R2}). (E) SEM derived largest particle dimension ("size") distribution histograms of the MNPL collected from the first extrusion of PP, HDPE and LLDPE. (F) The average molar mass (M_w) of the virgin along with bulk and MNPL collected after the first extrusion of PP, LLDPE, and HDPE. Error bars (some smaller than the data points) are the standard deviation of at least 3 measurements of MNPL collected from over 5 samples. Figures S9, S10, S12, S13, S14 present additional characterization results.

MNPL are highly polydisperse in both size and shape (and generally are far from spherical). While even these low mass fractions would translate into substantial quantities of MNPL at industrial scales, under laboratory conditions, this yields only sample masses of <0.1 mg, which makes further characterization difficult. Since the use of accelerated protocols has previously been proven to be effective for studying MNPL generation mechanisms (1), we apply a similar strategy to obtain sufficient material for detailed characterization. PP, HDPE, and LLDPE are subjected to melt extrusion at 200 °C, at 21 rad/s for 15 min (Methods Table S1). (The corresponding data for the three other polymers studied are presented later). We first examine PP. Upon bringing the extrudate into contact with water, the supernatant exhibited even higher light scattering count rates than those observed after shorter extrusion time (Figures 1A, S4, S5). Solvent evaporation, followed by vacuum drying at 40 °C for 12 h, yields a white MNPL powder (1 % of total polymer mass), which was

subsequently used for further characterization (Figures 1C).

Energy-dispersive X-ray spectroscopy (EDS), ATR-FTIR and HT-SEC were employed to distinguish polymer-derived material from common additives, including antioxidants and waxes in the MNPL. Their elemental composition reflects only carbon and oxygen (Figure S6), ruling out inorganic fillers or mineral-based additives within EDS detection limits (28). ATR-FTIR spectra revealed characteristic polyolefin signatures, including C–H stretching bands between 2841 cm^{-1} and 2955 cm^{-1}, corresponding hydrocarbon absorptions in the fingerprint region (29), and 1600 cm^{-1} to 1800 cm^{-1} carbonyl bands (30) which support the existence of oxygenated hydrocarbons (Figures 1D, S3 to S10). No distinct spectral features associated with nitrogen, phosphorus or phenol containing functional groups were found, suggesting that amide or phosphite-based additives (e.g., slip agents (28) and antioxidants (31)) were not dominant contributors. Further, HT-SEC revealed that the molar mass distribution of the MNPL was unimodal, indicating a single dominant population of chain fragments (Figures S9, S10). Thus, the formation of MNPL is not attributed to additives. To further corroborate this conclusion, an identical extrusion protocol was applied to additive-free PP which also yielded MNPL (Figure S11). These results confirmed that, irrespective of residence time, extrusion speed, or polymer grade (additive-free or commodity), routine processing of PP consistently generates polymer-derived MNPL with the same qualitative characteristics (Figures 1B–D, S2, S3, S11).

Applying the same protocol to the HDPE and LLDPE revealed that the MNPL collected after the first processing cycle exhibited a broad distribution of sizes and morphologies (Figures 1E, S9, S10). Since the largest-dimension distributions are non-Gaussian, the data is reported as the median (interquartile range, IQR), calculated using Equations S3–S6, rather than as the mean and standard deviation (32). The largest dimensions of the MNPL were [0.56 (IQR, 0.47)] μm for PP, [1.77 (IQR, 2.45)] μm for LLDPE, and [6.09 (IQR, 6.63)] μm for HDPE (Figure 1E), respectively, with the particle widths and heights being smaller (100 nm - 1 μm range). These size differences across different polymers are likely governed by reaction kinetics, influenced by factors like radical stability, susceptibility to crosslinking, initial molar mass and steric hindrance (33–36). MNPL produced by polymers subjected to an additional extrusion cycle exhibited a reduction in average size and dispersity, e.g., for PP the MNPL sizes drop to [0.29 (IQR, 0.19)] μm (Figure S12).

Next, the structure of the MNPL was compared to the corresponding processed, bulk polyolefins. While the polyolefins, after the first and second processing cycles, showed minimal oxidative functionalization, as evidenced by weak infrared FTIR absorption in the 1600 cm^{-1} to 1850 cm^{-1} region (30, 37–39), the corresponding MNPL exhibited significantly higher oxidation levels (Figures 1D, S9, S10, S13). Further, HT-SEC revealed a reduction in the bulk polymer molar mass after processing, with PP exhibiting a substantially greater decrease than PE after the first processing cycle, consistent with the greater susceptibility of PP to chain scission and of PE to crosslinking (Figures 1F, S9, S10, S13, S14) (37, 40, 41). The mass averaged

molar mass, M_w, of the MNPL are approximately an order of magnitude lower than that of the corresponding bulk material (Figures 1F). For example, PP-derived MNPL from the first processing cycle have M_w = (23 ± 2) kDa, compared to (153 ± 4) kDa for the bulk extruded PP. The MNPL were consistently enriched in lower molar mass, more highly oxidized polymer relative to the bulk extruded material (Figures S9, S10, S13).

Release of MNPL under Quiescent Conditions: Quiescent high-temperature oxidation was used to decouple the effects of temperature and shear. These experiments are inspired by Bueche (42), who posited that: "If one considers the action of oxygen only in so far as it aids bond scission and ignores its effects upon other reactions, the effect of oxygen is nearly equivalent to reducing the energy needed for bond rupture." Since flow fields reduce the bond scission energy, phenomenologically, the two situations should yield similar results, with the simplification that quiescent conditions do not impose complex flow fields. Importantly, the quiescent degradation work here is fundamentally distinct from the quiescent solid-state oxidation of PP and PS reported by Mendez et al. (1). That study showed MNPL formation through chain scission in the amorphous regions of semicrystalline polymers, ultimately releasing crystalline domains into the environment. Instead, the present study investigates polymers in the melt where there is no such underlying morphology.

PP samples were sealed in vials and heated in a reaction block below T_m, at 150 °C, and above T_m at 200 °C and 240 °C, respectively, for up to 24 h, and then quenched to room temperature. Under these conditions, the film surface exhibited both micro and macroscopic cracking, along with the formation of loosely attached particles which are readily suspended into water (Figures 2A, S15). In parallel, a measurable mass loss (up to 7 % ± 2 %) was observed, which is attributed to volatile organic compounds (VOCs) (43–45) and MNPL (Figure S16). Light scattering only confirms the presence of MNPL in the water (1), as VOCs do not contribute significantly to scattering. A pronounced increase in both mass loss and count rate was observed for samples oxidized above T_m relative to those below T_m (Figure 2B). Moreover, irrespective of reaction conditions, the light scattering count rate collapses onto a single linear trend with mass loss, apparently suggesting a common underlying scission-controlled mechanism governing both VOC formation and MNPL release (Figure S16).

To characterize the MNPL formed, we used a protocol similar to the one for the extruded samples. SEM of this residue showed that, at earlier stages of the reaction (corresponding to lower reaction temperatures and shorter reaction times), the particles exhibited highly polydisperse sizes and shapes (Figures S17 to S21). As the reaction progresses, the size distribution narrowed, with spindle-shaped MNPL being the dominant morphology (Figures 2C, 2D). The particle size (longest dimension) was [0.94 (IQR, 0.68)] μm, [1.08 (IQR, 0.46)] μm, and [0.64 (IQR, 0.24)] μm, after 24 h at 150 °C, 200 °C, and 240 °C, respectively (Figures 2D, S22). Similar to the extruded samples, ATR-FTIR revealed that the MNPL collected from PP samples quiescently oxidized above T_m, also contained carbonyl functionalities (Figures 2E, S23). ^{1}H NMR

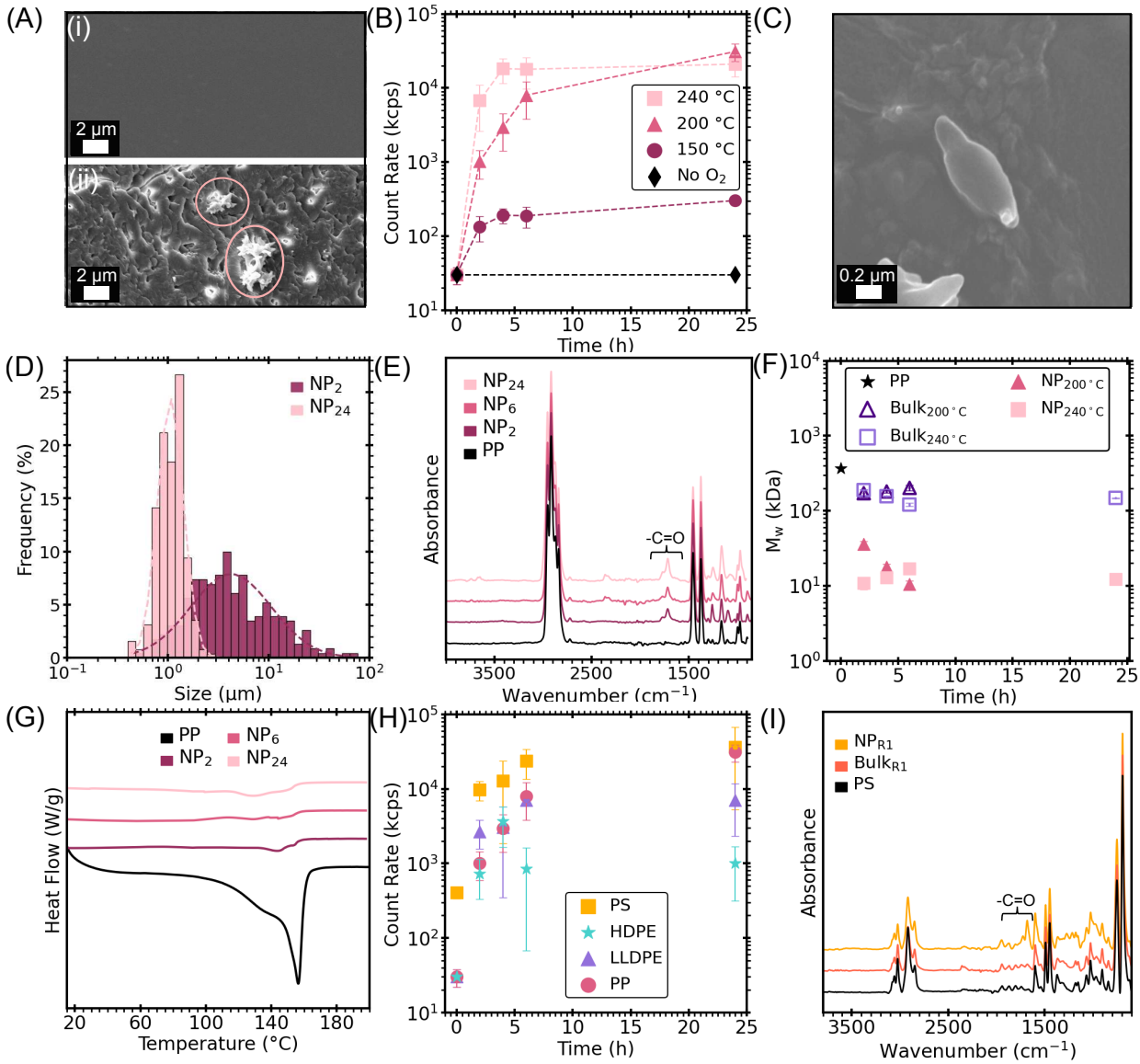


Figure 2: **Properties of MNPL Recovered from Quiescent Polymer Oxidation.** (A) SEM micrographs of the surfaces of (i) unoxidized and (ii) oxidized samples. (B) Light scattering count rate at an angle of 175 ° of the supernatant water collected from oxidized samples as a function of time up to 24 h for PP oxidized at 150 °C, 200 °C and 240 °C, respectively. Note: light scattering on PP heated at 200 °C in the absence of oxygen for 24 h is added as a control (labeled no O_2). (C) SEM micrograph of a single spindle-shaped MNPL recovered from PP oxidized at 200 °C for 24 h. (D) Size distribution histograms obtained from image analysis of SEM micrographs for MNPL collected from PP oxidized at 200 °C for 2 h (labeled NP_2) and 24 h (labeled NP_{24}). The distributions were fitted with lognormal functions (R^2 reported in the SI). Note: the reported size corresponds to the longest dimension. (E) ATR-FTIR spectra of MNPL (labeled NP_x) recovered from PP oxidized at 200 °C after x hr. Data for virgin PP is shown for comparison. (F) M_w of the bulk and MNPL collected after oxidation at 200 °C ($Bulk_{200\ ^\circ C}$ and $NP_{200\ ^\circ C}$ respectively), and 240 °C ($Bulk_{240\ ^\circ C}$ and $NP_{240\ ^\circ C}$ respectively). Error bars (some smaller than the data points) are the standard deviation of at least 3 measurements of MNPL collected from over 20 samples. (G) DSC second heating curves for MNPL (labeled NP_x) recovered from PP oxidized at 200 °C after x hr. The virgin PP reference is also shown for comparison. (H) Light scattering count rate at an angle of 175 ° as a function of time for HDPE, LLDPE, PP and PS at 200 °C. (I) ATR-FTIR spectra of PS MNPL and bulk recovered from the first extrusion in comparison to virgin PS.

displayed characteristic peaks at 4.74 ppm and 4.82 ppm for terminal vinylidene groups, 2.15 ppm for methyl ketones, 9.67 ppm for aldehydes, and 4.93 ppm and 4.97 ppm for in-chain alkenes (Figures S24, S25) (30, 35, 46). Most carbonyl groups formed at the chain ends, with the average number of carbonyl groups per chain, calculated using Equation S11, ranging from 0.78 ± 0.03 to 1.71 ± 0.02 across the conditions studied (Figure S26). Further, MNPL molar mass distributions were close to an order of magnitude lower than the corresponding bulk, for all the reaction temperatures and times (Figures 2F, S27, S28).

SAXS/WAXS and DSC were employed to study the crystalline structure of the MNPL. While the MNPL largely preserved the α-form of the bulk PP, WAXS reflections corresponding to the γ plane reflection (117) also begin to appear (47) (Figure S29). Moreover, the MNPL displayed disrupted long-range order and the absence of lamellar stacking since there is no long period SAXS peak (Figures S29, S30). While the MNPL retains its semicrystalline structure, also confirmed by the presence of 998 cm^{-1} and 973 cm^{-1} FTIR bands (4, 48) (Figure 2E), it demonstrates a sharp depression in both crystallinity and melting temperature, reaching an average value of (10 ± 5) % and (132 ± 5) °C, respectively, across the various oxidation temperatures and times (Figures 2G, S31). This is expected given the oxidative defects in the MNPL chains which disrupt the crystal structure (30). Further, the MNPL exhibited reduced thermal stability compared to the bulk polymer, with degradation temperatures ranging from (253 ± 11) °C to (330 ± 14) °C, in contrast to (380 ± 10) °C for bulk PP (Figures S32, S33). The reduction in thermal stability is likely due to the presence of oxidised species. Moreover, a selective lack of certain antioxidants, which are present in bulk polymer, could be relevant.

Light scattering was used to measure the relative concentrations of MNPL produced from the quiescent oxidation of LLDPE and HDPE relative to that from PP at 200 °C. After 24 h, the extent of MNPL released followed the trend PP > LLDPE > HDPE, as found above for the extruded samples (Figure 2H).

MNPL Release from Processed Amorphous Non-Polar Polymers: To test if these observations are only limited to semicrystalline polymers, the quiescent oxidation and extrusion of amorphous polystyrene (PS), another hydrocarbon polymer, was studied. Virgin PS pellets contacted with water exhibited increasing light scattering (Figure 2H), likely driven by the intrinsic brittleness of the material ($T_g \approx 100$ °C (49)), which renders it susceptible to fragmentation even under mild stresses such as pellet–pellet rubbing during handling. Following quiescent thermal oxidation, the light scattering counts increase, approaching that of PP by 24 h (Figure 2H). (Extrusion yielded similar results, Figure S34.) Moreover, consistent with the semicrystalline polyolefins, PS MNPL recovered were more oxidized than their bulk processed counterparts (Figure 2I).

MNPL Release from Processed Oxygen Containing Polymers: To examine the generality of these ideas, we extrude nylon-6 and bisphenol-A-polycarbonate, the former a semicrystalline polymer, while the latter an amorphous, high glass transition temperature plastic. These materials were subjected to extrusion

at 250 °C and 220 °C, respectively, for 5 min and 15 min. The polymers were cooled and then contacted with water. As with the non-polar polymers, an increase in light scattering counts was observed with increasing processing time (Figure S35). Taken together, these results demonstrate that both polar and non-polar, semicrystalline and amorphous polymers release MNPL on melt-processing.

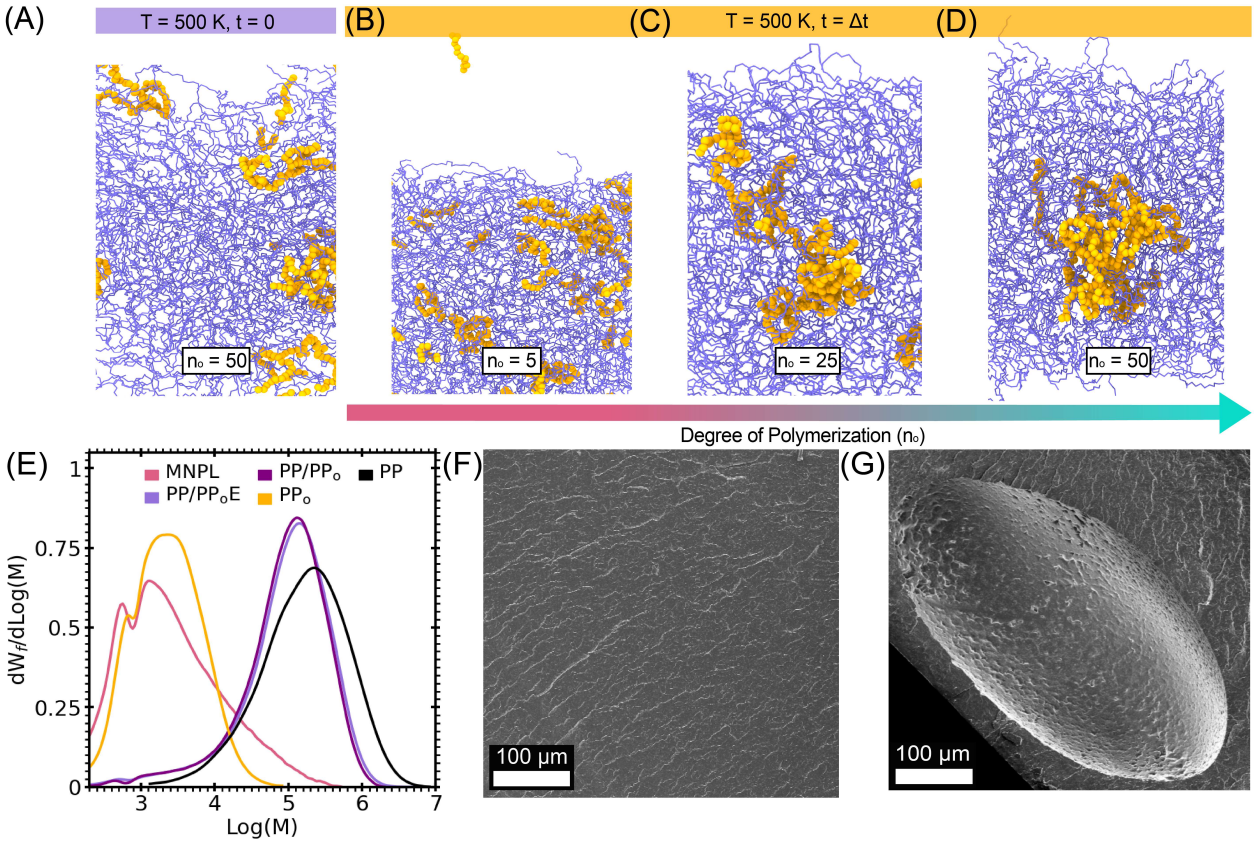


Figure 3: **MD Snapshots of PE Chains Mixed with Short Oxidized PE Chains and Experimental Data for PP Analogs**. Top row - MD simulations. PE_o monomers are represented as yellow beads; violet lines correspond to PE chains. The polymer–air interfaces are located at the top and bottom of each snapshot. Periodic boundary conditions are applied along the left and right sides of each snapshot. (A)-(D) all have PE chains of length 100, which were mixed with PE_o with a mass fraction of w = 5 % at T= 500 K. (A) initial melt-mixed system PE/PE_o (100/50) (time, t = 0). (B)-(D) Equilibrated systems containing PE_o chains of different lengths: (B) n_o = 5, (C) PE_o = 25 and (D) PE_o = 50. Bottom row - Experimental data. (E) Molar mass distributions of virgin PP, PP_o along with PP/PP_o (90/10) extruded blend before extraction (labeled PP/PP_o) and after the extraction (PP/PP_oE) of MNPL. The molar mass distribution of the MNPL recovered is also plotted. SEM micrographs of cryofractured cross-sections of melt-mixed PP/PP_o blends containing PP_o mass fractions of (F) 1 wt% and (G) 20 wt%, respectively.

Mechanistic Understanding of MNPL Release Driven by Phase Separation: To elucidate the mechanism underpinning the release of MNPL, MD simulations and complementary experiments were used. MD simulations were conducted on polymer films using the Groningen Machine for Chemical Simulations (GROMACS) package with the Optimized Potentials for Liquid Simulations (OPLS) all atom force field

(50, 51) (Figures S36). Since we are primarily interested in the "universal" physics underpinning the MNPL formation, we hypothesized that the essential driver must arise from the fact that extrusion/oxidation yields chains that are shorter and carry an oxidized functionality. Guided by this hypothesis, we simulated mixtures comprising long unfunctionalized PE chains mixed with a small fraction of short oxidized chains. Our objective is not to model the detailed chemistry of chain scission, oxidation, or competing side reactions such as crosslinking, nor the precise locations of oxidized functionalities along the chains. Instead, we sought to identify the bulk and surface behavior that emerges when polymer chains which differ in both length and chemical functionality, are mixed in the bulk and cooled below their melting points (Figures S36). We first examine the resulting behavior in the melt phase.

To isolate the effect of disparity in chain lengths, a system comprising PE chains with a degree of polymerization n = 100, capped at both ends by methyl groups, was mixed with short PE chains (n = 25). In the melt (500 K), these chains are miscible, as expected. On cooling, these short chains cocrystallize with the long chains (Figure S37, S38). Next, to account for the effects of oxidation, unfunctionalized PE chains with a degree of polymerization, n = 100 were mixed with telechelic oxidized PE chains (PE_o) with n = 5, 25 and 50, respectively, with a mass fraction (w) of (1 to 5) % (Figure 3A). The blends were labeled PE/PE_o n/n_o, where n and n_o are the degrees of polymerization of PE and PE_o, respectively. Five independent simulation repeats were performed for each system. Note that PE_o chains shorter than n = 25 are prone to volatilizing at 500 K (Figure 3B, S39). Regardless, PE/PE_o (100/5 and 100/25, w = 5 %) simulated in the melt state (500 K) exhibited no evidence of macrophase separation (Figures 3B, 3C). In contrast, simulation of a PE/PE_o (100/50, w = 5 %) blend displayed the presence of PE_o-rich phase separated domains, across the compositions studied (Figure 3D, S40, S41). Snapshots confirmed that the observed phase behavior does not correspond to microphase separation. To provide a thermodynamic framework for interpreting this behavior, we present a supporting Flory analysis in the discussion of Equation S14. This suggests that PE_o needs to be of a critical chain length for phase separation, which in this case appears to be near n = 25.

To experimentally probe the predicted phase separation between oxidized chains and virgin polymer, PP_o was synthesized via quiescent oxidation as described in our earlier work (30), and subsequently melt-mixed with virgin PP for less than 2 min to minimize additional extrusion-induced degradation (Figures 3E). The oxidative functionality and crystallinity of PP_o were designed to closely match those of the experimentally collected MNPL, with an average $f_o = 1.48 \pm 0.08$ oxidized functional groups per chain and crystallinity $X_c = (12 \pm 5)$ %, respectively, while maintaining a comparably narrow molar mass distribution (Figures 3E, S42, S43 and Table S5). Increasing the PPo mass fraction in PP/PPo blends led to macroscopic phase separation, consistent with the MD predictions (Figures 3F, 3G).

The observed bulk phase separation is expected to compromise the mechanical integrity of the processed

polymer. Commercial PP is both ductile and tough under uniaxial tension at room temperature, exhibiting a Young's modulus of $E = (773 \pm 157)$ MPa. Upon extrusion (labeled Bulk_{R1} in Figure 4E), the bulk mechanical properties, especially ductility and toughness, deteriorate. This effect is further pronounced on second extrusion (Bulk_{R2}). While the semicrystalline morphology (crystallinity and long period) experience negligible change after the first and second extrusion, the deterioration of mechanical properties can be attributed to increasing oxidation levels leading to increasing phase separation and embrittlement.

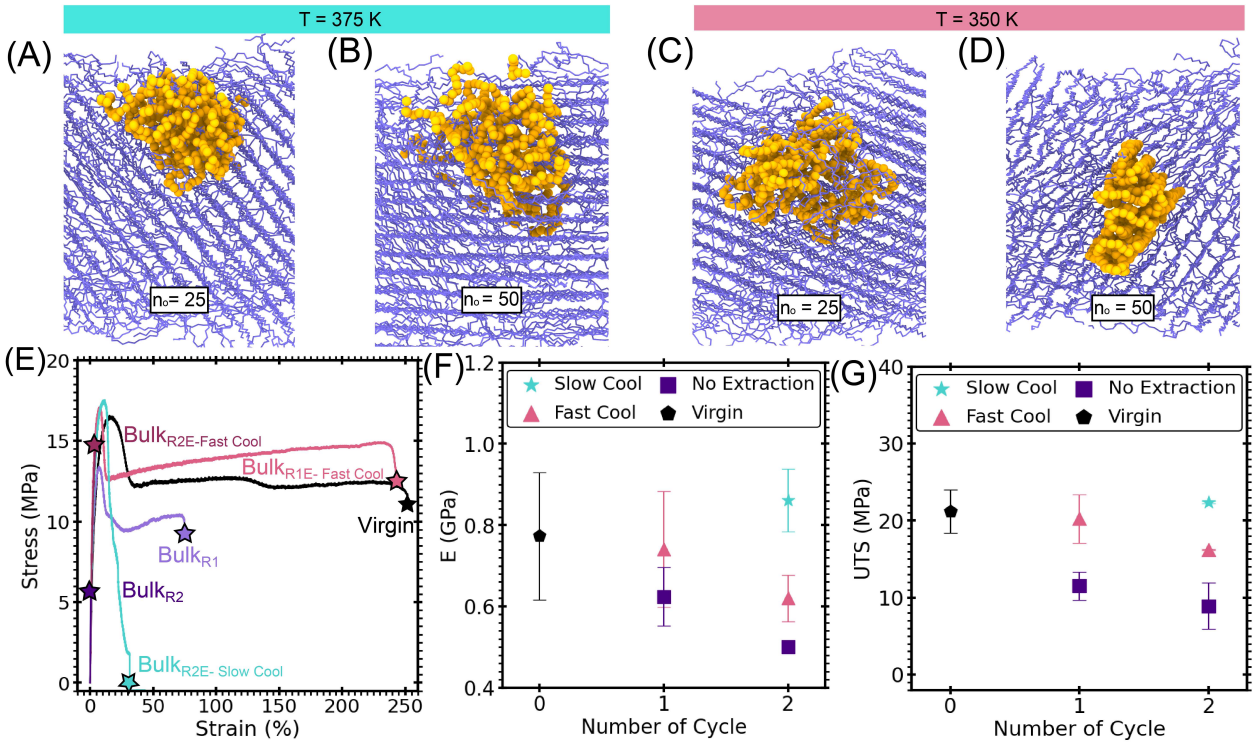


Figure 4: **MD Simulations of Crystallization Driven Defect Transport and Their Experimental Consequences on Mechanical Properties.** Top row - MD simulations. PE_o monomers are represented as yellow beads; violet lines correspond to PE chains. The polymer–air interfaces are located at the top and bottom of each snapshot. Periodic boundary conditions are applied along the left and right sides of each snapshot. The system has PE chains with n = 100, and are mixed with PE_o (mass fraction, w = 5 wt%). The systems were annealed at 500 K and quenched to (A, B) 375 K or separately to (C, D) 350 K. (A) and (C) refer to PE_o of length $n_o = 25$, while (B) and (D) are for $n_o = 50$. Bottom row - Experimental data. (E) Uniaxial tensile stress-strain curves for the virgin PP (Virgin) with bulk polymer processed once (Bulk_{R1}) and twice (Bulk_{R2}). These controls are compared to the mechanical properties of the bulk polymer post the fast cool extraction of MNPL ($\text{Bulk}_{\text{R1}-\text{Fast Cool}}$ and $\text{Bulk}_{\text{R2}-\text{Fast Cool}}$) and the slow cool extraction of MNPL ($\text{Bulk}_{\text{R2}-\text{Slow Cool}}$). Note: The star in each stress–strain curve indicates the fracture point. (F) Young's Modulus and (B) Ultimate tensile strength (UTS) of the different samples. Error bars (some smaller than the data points) are the standard deviation of at least 5 measurements.

Does Crystallization Additionally Drive MNPL Creation? While oxidation induced phase separation is prone to occur in these systems, MD simulations further show that, in the melt, the resulting PE_o-rich phase remains largely confined to the film interior in the melt, away from the interface. This is consistent

with the higher surface energy of the oxygenated moieties (52), which renders them interfacially inactive (Figures 3C, 3D). This result also implies that the chain entropy which would otherwise drive short chains to the surface is a weaker effect than oxidation induced enthalpic effects for most realistic chain lengths (53).

We therefore hypothesized that the surface segregation of these short, oxygenated chains to form MNPL, occurs during cooling from the melt into the semicrystalline state. This ansatz was tested using both MD and complementary experiments. Previously, Keith and Padden examined how polymer crystallization dealt with non-crystalline "defects" (54). These workers argued that during crystallization, defects were moved a distance $\delta = \frac{D}{G}$ where D is the defect diffusivity and G is the crystal growth velocity. While the former quantity varies with temperature with an essentially Arrhenius dependence, the G has a much stronger $exp\left[-\frac{C}{\Delta T}\right]$ dependence, where C is a constant and ΔT is the undercooling (54). Thus, we postulated that varying the G through controlled changes in ΔT could cause the defects near the air surface to segregate to it, especially for small undercoolings. Indeed, in the simulations, isothermal crystallization at 375 K enabled PE_o chains to segregate toward the polymer–air interface with a high probability (Figures 4A, 4B, S40, S45, S48). In contrast, upon crystallizing at 350 K, where the G values is expected to be much higher, the functionalized chains more likely became kinetically trapped within the bulk and remained confined there (Figures 4C, 4D, S40, S46). This effect was observed independent of the mass fraction or degree of polymerization of PE_o added.

To experimentally validate this idea, PP recovered after the first and second melt-processing cycles was subjected to MNPL extraction protocols discussed above. The remaining polymer was then melt-pressed (quenched), to ensure the samples had the same thermal history, and subjected to uniaxial tensile testing. The bulk mechanical properties after removing the surface skin layer following the first extrusion cycle ($Bulk_{R1E-Fast\ Cool}$) were notably improved. In particular, the modulus, ultimate tensile strength, the strain to break and toughness all assume values close to the unprocessed bulk. This can be attributed to the removal of a weakly adherent surface layer composed predominantly of short oxidized chains, which would otherwise remain phase separated within the material (Figures 4E- 4G, S49, S50). These property improvements are significantly less pronounced in materials subjected to a second processing cycle. This behavior may arise because of larger fraction of phase separated material is created which remains kinetically trapped in the bulk ($Bulk_{R2E-Fast\ Cool}$). Consequently, while both the modulus and ultimate tensile strength still show improvements, the strain to failure and toughness remain essentially unchanged relative to $Bulk_{R2}$ (Figures 4F, 4G, S50). FTIR studies show no measurable differences in oxidation levels and crystallinities for these extracted samples, rationalizing these findings.

To further improve the properties of $Bulk_{R2}$, guided by MD simulations, PP reprocessed the second time was subjected to a slow cool MNPL extraction followed by measurement of its mechanical properties. To do so, the extrudate was collected and annealed in vacuumn at 180 °C for 5 min and allowed to slow cool to room

temperature at the rate of $\approx 0.5\ ^{\circ}\mathrm{C\,min^{-1}}$. Then the polymer was subjected to MNPL extraction followed by melt-pressing (quench) and mechanical testing. $\mathrm{Bulk_{R2E-Slow\ Cool}}$ showed a gentle improvement in both toughness and elongation at break in comparison to $\mathrm{Bulk_{R2E-Fast\ Cool}}$ but was successful in recovering both the modulus as well as the ultimate stress of the unprocessed polymer (Figures 4F, 4G, S50).

Conclusions: We demonstrated that melt-processed polymers released MNPL into contacting water. This unexpected source of MNPL has been demonstrated across a diverse range of polymers, including three semicrystalline polyolefins, one amorphous hydrocarbon and two oxygen containing polymers (one amorphous and one semicrystalline). The recovered MNPL consisted predominantly of short, oxidized fragments, presumably formed by chain scission. Through a combination of MD simulations and complementary experiments, it was established that these short oxidized chains have a propensity to phase separate from the undegraded polymer matrix. This phase behavior, together with crystallization-driven transport, governed both their retention in the bulk and their selective enrichment at interfaces, leading to MNPL formation. This phase separation also contributes to the progressive deterioration in mechanical properties relative to their virgin counterparts. Importantly, crystallization can thus be harnessed to drive surface segregation of some of these fragments, offering a potential route for their mitigation at source and for improving the performance of these classes of extruded polymers.

Supporting Information Characterization of MNPL collected from short time extrusion; light scattering of the water in contact with the extruded samples; PE MNPL collected from after extrusion; MNPL collected from additive-free PP; MNPL from PP after multiple extrusions; quiescent oxidation of PP; MNPL produced from extruded PS; MNPL produced from extruded oxygen containing polymers; MD simulations; Flory-Huggins predictions of miscibility; $\mathrm{PP_o}$ characterization; bulk mechanical properties.

Author Contributions S.D. performed the experiments (PP, HDPE, LLDPE, PS), wrote, compiled and edited the manuscript. J.A. performed the MD simulations. A.B. performed the HT-SEC measurements and manuscript editing. A.M performed the tests for oxygen containing polymers. T.P and G.K. aided in discussion and editing of the manuscript. S.K.K. conceived the project, and wrote and edited the manuscript.

Acknowledgement The authors thank Dr Carlos Lopez-Barron (ExxonMobil) for providing the additive-free PP. Matthew J. Campen (Univ of New Mexico), Mark Wiesner (Duke University), Linda S. Schadler (Univ of Vermont), Alejandro J. Müller (San Sebastian), and Dr. Michele Valsecchi (Columbia University) reviewed the draft and provided many important comments and insights. Dr. Jeff Weinhold (Dow) provided us important information about a PP wax in the commercial PP samples that could affect the results obtained. We thank Dr Sainath Vaidya from Envalior for providing the PA6 and Dr H. V. Pol from CSIR-National Chemical Laboratory for the BPA-PC. This material is based upon work supported by the U.S. Department of Energy, Office of Science, Basic Energy Sciences under Award Number DE-SC0023281.

Notes Certain equipment, instruments, software, or materials are identified in this paper in order to specify the experimental procedure adequately. Such identification is not intended to imply recommendation or endorsement of any product or service by the National Institute of Standards and Technology (NIST), nor is it intended to imply that the materials or equipment identified are necessarily the best available for the purpose. Moreover, the content is solely the responsibility of the authors and does not necessarily represent the official views of the National Institutes of Health.

Competing Interests The authors declare no competing interests.

Methods

Materials: The PP was purchased from Sigma Aldrich as films of thickness $L = 496$ μm (as measured by a vernier caliper). The polymer has $M_w \approx 369$ kDa and number-average molar mass $M_n \approx 62$ kDa ($Đ = 5.9$) as determined by HT-SEC. It has a crystallinity of 32 % and a melting point of 158 °C as determined by DSC. Antioxidant-free PP was graciously provided by ExxonMobil. The LLDPE pellets were purchased from Sigma Aldrich with a $M_w \approx 97$ kDa and $M_n \approx 18$ kDa ($Đ = 5.3$). It has a crystallinity of 33 % and a melting point of 114 °C. The HDPE pellets were purchased from Goodfellow, $M_w \approx 70.5$ kDa and $M_n \approx 16.1$ kDa ($Đ = 4.9$). It has a crystallinity of 78 % and a melting point of 135 °C. Nylon, PA-6 was provided by Envalior, and is characterized by MVR 30 (235 °C/2.16 Kg) with a relative solution viscosity of 2.3 (in 96% sulphuric acid). BPA-polycarbonate, Lexan 143R (MVR = 12 cc/10 min at 300 °C/1.2 Kg), was provided by CSIR-National Chemical Laboratory. 1,1,2,2-Tetrachloroethane-d_2 ≥ 99.5 and dichloromethane (dcm) were purchased from Sigma Aldrich and HPLC grade 1,2,4-trichlorobenzene was purchased from J.T. Baker.

Table 1: Sample naming conventions with description

Variable Name	Description
$Bulk_{R1}$	Bulk sample collected after the first extrusion, before MNPL extraction
$Bulk_{R2}$	Bulk sample collected after the second extrusion, before MNPL extraction
$Bulk_{R1E-Fastcooled}$	Bulk sample collected after the first extrusion, fast cool MNPL extraction
$Bulk_{R2E-Fastcooled}$	Bulk sample collected after the second extrusion, fast cool MNPL extraction
$Bulk_{R2E-Slowcooled}$	Bulk sample collected after the second extrusion, slow cool MNPL extraction
NP_{R1}	MNPL sample collected after the first extrusion
NP_{R2}	MNPL sample collected after the second extrusion
NP_2	MNPL sample collected after quiescent oxidation at 200 °C for 2 h
NP_4	MNPL sample collected after quiescent oxidation at 200 °C for 4 h
NP_6	MNPL sample collected after quiescent oxidation at 200 °C for 6 h
NP_{24}	MNPL sample collected after quiescent oxidation at 200 °C for 24 h
$NP_{200°C}$	MNPL sample collected after quiescent oxidation at 200 °C
$NP_{240°C}$	MNPL sample collected after quiescent oxidation at 240 °C
$Bulk_{200°C}$	Bulk sample collected after quiescent oxidation at 200 °C
$Bulk_{240°C}$	Bulk sample collected after quiescent oxidation at 240 °C
PP/PP_o	Bulk sample collected after the extrusion of a 90/10 PP and PP_o blend.
PP/PP_oE	Bulk sample collected after the extrusion of a 90/10 PP and PP_o blend, MNPL extracted

MNPL Production by Extrusion: PP, HDPE, and LLDPE films/pellets were cleaned with acetone whereas PS pellets were cleaned with HPLC water to remove surface dust and subsequently degassed in a vacuum oven at 60 °C for 12 h. Melt extrusion was carried out using a HAAKE Standard MiniLab 3 Micro Compounder equipped with a conical co-rotating screws. Prior to extrusion, the extruder temperature was stabilized at 200 °C for 1 h and the extruder was purged thrice using the polymer to be extruded. The polymer (≈ 5 g) was then fed into the hopper and recirculated through the backflow channel for 5 or 15 min at different speeds. The extrudate was collected, cooled to room temperature and contacted with

water. This supernatant water was then used for light scattering. Alternately, other solvents were also used for the extraction of MNPL (dichloromethane for polyolefins and water for PS), with a contact time of <1 min. Note that these solvents produced no particles when brought in contact with virgin polymers (Figure S5). The resulting supernatant was poured into glass petri dishes and allowed to evaporate under ambient conditions. The residue was then vacuum dried at 40 °C for 12 h, yielding a white powder, used for further characterization.

Nylon-6 and BPA-PC were initially washed using distilled deionized water and then vacuum dried at 100 °C overnight. The polymers were then extruded using a DSM-5 twin-screw batch extruder operated in a vertical configuration and equipped with co-rotating conical screws. The extruder temperature was set as required (250 °C for nylon-6 and 220 °C for BPA-PC), and was allowed to stabilize over 15 minutes. Prior to each run, the extruder was purged using the polymer to be extruded. About (4-5) g of the polymer was fed into the extruder, operated at a screw speed of 21 rad/s and the extruder was run in recycle mode for the desired time (5 min or 15 min). Samples were then collected in a glass beaker. After cooling, 500 mg of the sample was weighed and brought in contact with filtered distilled deionized water, and the dispersion was used for light scattering tests.

MNPL Production by Quiescent Oxidation: For the quiescent thermal oxidation experiments, 500 mg of films/pellets were cleaned and degassed in a vacuum oven at 60 °C for 12 h. PP, HDPE, and LLDPE films/pellets were cleaned with acetone whereas PS pellets were cleaned with water to remove surface dust. Glass vials (4 mL) were rinsed at least three times with acetone to minimize dust contamination. The polymer was transferred into the vials, which were sealed using polytetrafluoroethylene tape. The sealed vials were placed in a 1 dram (4 mL) vial reaction block (15 mm × 45 mm) for thermal oxidation. Oxidation was conducted at fixed temperatures of 150 °C, 200 °C, and 240 °C, respectively, for reaction times up to 24 h. Following oxidation, the sealed vials were cooled to room temperature and contacted with water. This supernatant water was then used for light scattering. Alternately, other solvents were used for extraction of MNPL (dichloromethane for polyolefins and water for PS). The vials were solvent contacted for <1 min, after which the supernatant was poured into glass petri dishes and allowed to evaporate. The resulting residue was vacuum dried at 40 °C for 12 h.

Light Scattering: Light scattering measurements on PP, HDPE, LLDPE and PS samples were performed using a Malvern Zetasizer Nano ZS and disposable poly(methyl methacrylate) cuvettes. The detector scattering angle was 175 °, and the temperature was controlled at 25 °C. Following quiescent oxidation, the sealed vials (containing 500 mg polymer) were cooled to room temperature, and 1 mL water was added to the vial. For the extruded samples, 500 mg of the extrudate was collected and 1 mL water was added to it. Light scattering was then performed on the supernatant water collected to measure the increase in count rate

without employing any attenuation protocol. Derived count rates are reported to account for the number of particles. The error bars were the standard deviation of three independent repeats.

For the MNPL samples from BPA-PC and Nylon-6, light scattering measurements were performed using a Litesizer 500 DLS (Anton Paar). Samples were loaded into quartz cuvettes, the scattered intensity was measured at 15 ° and the temperature was 25 °C. We note that the trends observed for the scattered counts at 175 ° were similar to those reported here. The error bars are based on the standard deviation of the values from three independent experiments.

Scanning Electron Microscopy (SEM): The surface of the quiescently degraded bulk films, the MNPL collected from extrusion and quiescent degradation, as well as the phase separated samples obtained by melt-mixing oxidized PP (PP_o) with PP, were analyzed using SEM. For imaging MNPL collected, the dried powder was deposited on the flat-top SEM stubs using carbon tape. The samples were then blown with air to remove loose material. For imaging the quiescently degraded bulk surface, samples were mounted on flat-top SEM stubs using carbon tape. For imaging PP/PP_o blends, the sample was immersed in liquid nitrogen for $\approx$ 20 min and then manually cryofractured. The samples were then mounted on 90 ° SEM stubs using carbon tape. All samples were sputter coated with Au/Pd (80/20) using a Safematic CCU-010 to deposit a 2 nm conductive layer. Imaging was performed using a Zeiss Sigma VP SEM at an accelerating voltage of 5 kV. Image analysis was carried out using ImageJ to determine particle size distributions from SEM micrographs. The longest dimension of each particle was measured, and over 200 measurements were collected for each reaction temperature, time, and shear condition across at least 20 samples.

Thermogravimetric analysis (TGA): Thermal degradation of the samples was conducted using a TA Instruments TGA 550. The experimental procedure first involved ramping to 700 °C at the rate of 20 °C/min in a nitrogen environment with a flow rate of 25 mL/min. Approximately 2 mg to 5 mg of the MNPL sample was placed on a platinum pan for the TG analysis. The mass loss at different stages was analyzed.

Differential Scanning Calorimetry (DSC): Thermal properties were measured using a TA Instruments Discovery 250 DSC. The instrument was calibrated using sapphire disks for heat capacity and indium for temperature and enthalpy. The sample chamber was always purged with nitrogen gas. The experimental protocol used for samples was a heat-cool-heat cycle which ramped at 10 °C/min from 0 °C to 240 °C followed by cooling at the same rate down to 0 °C and finally followed by another heating cycle to 240 °C at the same rate. The crystallinity (X_c) was calculated using the melting peak endotherm, Equation 1. For PP, $\triangle H_0$ was 207 J/g and that for PE was 286 J/g (55, 56).

$$\%X_c = \frac{\triangle H}{\triangle H_0} * 100 \tag{1}$$

Small and Wide Angle X-ray Scattering (SAXS and WAXS): X-ray scattering was performed using a SAXSLAB instrument equipped with a Cu Kα source with a photon energy of 8.04 keV ($\lambda = 1.54$ Å) at the Columbia University Soft Matter Laboratory. A moving Pilatus 300k detector with a variable sample-to-detector distance was used, covering a q range of 0.004–1.2 Å^{-1}. Scattering measurements were performed under vacuum at room temperature with an 1800 s exposure times. The resulting 2D detector images were processed and azimuthally integrated into 1D intensity profiles $I(q)$ using SAXSLAB's `saxsgui` software.

Attenuated Total Reflectance Fourier Transform Infrared Spectroscopy (ATR-FTIR): FTIR spectroscopy measurements were carried out with a Bruker Optics Tensor 27 FTIR spectrometer. The equipment was operated in ATR mode with 128 scans per sampling at a resolution of 16 cm^{-1} in the wavenumber range between 4000 cm^{-1} and 800 cm^{-1}. Spectra were filtered using the OMNIC software to account for artifacts caused by carbon dioxide and moisture in the air. A constant baseline was manually subtracted. The error bars in the carbonyl and vinyl index reported in Figure S23 is calculated from three independent measurements of the MNPL collected from more than 20 samples.

Nuclear Magnetic Resonance (NMR): Solution state ^{1}H NMR and ^{13}C NMR experiments were carried out on a 500 Ascent with the BB cryoprobe at high temperature (120 °C) in 1,1,2,2-Tetrachloroethane-d$_2$ (TCE-d$_2$, with ^{1}H NMR shift of 6 ppm and ^{13}C NMR shift of 73.78 ppm). The ^{1}H NMR has a ASTM signal to noise ratio (S/N) of 2417, and that for ^{13}C NMR is 1498. (10 ± 3) mg of the virgin polymer (finely cut into 10 to 15 pieces) or MNPL collected was subsequently added to (0.5 ± 0.2) ml of solvent in a glass vial. The glass vial was then sealed with Teflon tape and flushed with nitrogen for 30 min. Each sample was heated for 4 min to 5 min at 120 °C in an oil bath until the polymer completely dissolved. The sample was then transferred to air tight NMR tubes and bubbled with nitrogen. For ^{1}H NMR, 256 runs were performed with a relaxation time of 15 s, and for qualitative ^{13}C NMR, it was acquired over 664,400 runs with a relaxation time of 5 s. All ^{1}H NMR and ^{13}C NMR were processed and analyzed exclusively using TopSpin 3.6.2. The raw free induction decay (FID) data was first processed by applying exponential line broadening (LB = 1 Hz to 3 Hz) to enhance the signal-to-noise ratio, followed by a Fourier transformation (FT). After transformation, manual phase correction was performed with particular attention to both zero- and first-order phase parameters. Followed by that, manual baseline correction was performed. Then, the spectra were calibrated using the internal standard for the solvent TCE-d$_2$. Peaks were then manually picked, and integration was performed.

Multidetector High-Temperature Size Exclusion Chromatography (HT-SEC): HT-SEC was performed on a Polymer Char SEC-IR instrument containing an IR6 infrared detector. All measurements were performed using 1,2,4-trichlorobenzene (TCB) at 140 °C containing 300 mg/kg Irganox 1010 as the eluent and 3 Tosoh HT columns (1 Tosoh TSKgel GMHHR-H (20) HT2, 20 μL, 7.8 mm ID $\times$ 30 cm) column with an exclusion limit of approximately 4×10^8 g/mol as the stationary phase followed by 2 Tosoh

TSKgel GMHHR-H (S) HT2, 13 μL mixed bed, 7.8 mm ID $\times$ 30 cm columns). Samples were dissolved at a concentration of approximately 1 mg/mL. Sample vials were flushed with nitrogen, filled with 8 mL of eluent, and dissolved at 160 °C for 60 min with gentle agitation. Three injections from each sample vial were performed to obtain triplicate measurements. The sample injection volume was 200 μL. Samples were eluted at a flowrate of 1 mL/min. Narrow-dispersity polystyrene standards were used for column calibration. Calibration and data analysis were conducted with proprietary software from the instrument vendor. Molar masses were calculated by comparison to narrow polystyrene standards using appropriate Mark-Houwink-Sakurada (MHS) parameters as described in ASTM D6474-20. MHS parameters recommended by the instrument manufacturer were used for analysis ($\alpha_{PS} = 0.722$, $K_{PS} = 10.2$ μL/g , $\alpha_{PP} = 0.725$, and $K_{PP} = 19$ μL/g). Light scattering signal was low for low molar mass samples; therefore, the molar mass calculated from the PS standard calibration curve and MHS parameters was reported for all samples for consistency. The peak boundary for the analysis was set at an elution volume of no more than 32.0 mL, which corresponded to the elution volume of the lowest molar mass polystyrene standard (266 g/mol). This excludes lower molar mass fractions from the analysis which could lead to artificially higher molar mass and lower dispersity. The influence of oxidation and molar mass on MHS parameters was neglected.

Tensile Testing: The mechanical properties of the polymer samples were tested using a Chatillon CS2 testing machine with a 500 N load cell. The samples were melt-pressed at 200 °C, cooled to room temperature, subsequently forming free standing films. The films were cut into dogbone geometries using an ISO 527 type 5 A die. Samples were tested at a speed of 1 mm/min until failure. Engineering strain is calculated from the instrument displacement over the gauge length of the samples. Engineering stress is calculated using the pre-deformed cross-sectional area. The tensile measurements were averaged for at least 5 replicates, and samples that failed near the grips were not included in the averaging.

MD Simulations: Molecular dynamics (MD) simulations were performed on pristine polyethylene (PE) and carbonyl end-functionalized polyethylene (PE_o) mixtures with different chain lengths and compositions at 500 K, 375 K, and 350 K, respectively. The pristine PE system consists of linear PE chains with a degree of polymerization of 100 (PE), corresponding to $C_{200}H_{402}$. Three functionalized systems are constructed with chain lengths of 50, 25, and 5 respectively. Functionalization is introduced by replacing two terminal methyl groups with aldehyde groups. The blends were labeled PE/PE_o n/n_o, where n and n_o are the degrees of polymerization of PE and PE_o, respectively. For all the PE/PE_o systems, PE chains are mixed with PE_o in mass fractions of 1 %, 2 %, and 5 %. Initial bulk configurations are generated under periodic boundary conditions in all three directions. Each system is first equilibrated in the constant number of particles, pressure, and temperature (NPT) ensemble for 100 ns. Thin-film geometries are then created by extending the simulation box along the z-direction while keeping the x- and y-dimensions fixed, thereby introducing a

liquid slab surrounded by vacuum. The resulting films have lateral dimensions of approximately 6 nm to 7 nm and a z-dimension of 25 nm. The thin-film systems are subsequently simulated in the canonical (NVT) ensemble, in which the number of particles, volume, and temperature are held constant, at 500 K for 100 ns to obtain equilibrated melt structures. The systems are then quenched to 375 K and 350 K, respectively, followed by 1000 ns runs at each temperature. All simulations are performed using Groningen Machine for Chemical Simulations (GROMACS) (50) with the OPLS (Optimized Potentials for Liquid Simulations) (51) all atom force field. Bonds involving hydrogen atoms are constrained by the Linear Constraint Solver (LINCS) algorithm (57), and a time step of 1 fs is employed. Temperature is controlled using the velocity-rescaling (V-rescale) thermostat (58) for the NVT simulations with a relaxation time of 0.5 ps. We use the Parrinello-Rahman barostat (59) and Nosé-Hoover thermostat (60, 61) for the NPT simulations. The pressure is 1 atm for the NPT simulation with a relaxation time of 2 ps. The van der Waals and electrostatic interactions are truncated and shifted to zero for a cutoff distance of 1.2 nm. Further, long-range electrostatic interactions are calculated using the Particle Mesh Ewald (PME) (62) method.

References

[1] Mendez, N. F. *et al.* Mechanism of quiescent nanoplastic formation from semicrystalline polymers. *Nature Communications* **16**, 3051 (2025).

[2] Meides, N. *et al.* Reconstructing the environmental degradation of polystyrene by accelerated weathering. *Environmental science & technology* **55**, 7930–7938 (2021).

[3] Shen, H., Wang, X., Lee, A. K., Abbatt, J. P. & Chan, A. W. Nanoplastic particle emissions from plastic smoldering combustion. *Environmental Science & Technology* **59**, 19339–19350 (2025).

[4] Li, D. *et al.* Stress-induced phase separation in plastics drives the release of amorphous polymer micropollutants into water. *Nature Communications* **16**, 3814 (2025).

[5] Song, Y. K. *et al.* Combined effects of uv exposure duration and mechanical abrasion on microplastic fragmentation by polymer type. *Environmental science & technology* **51**, 4368–4376 (2017).

[6] Lee, H. *et al.* Fire-exposed polypropylene as a potential source of nanoplastics in aquatic environments. *Journal of Hazardous Materials* 140106 (2025).

[7] Song, Y. K., Hong, S. H., Eo, S. & Shim, W. J. Fragmentation of nano-and microplastics from virgin-and additive-containing polypropylene by accelerated photooxidation. *Environmental Pollution* **327**, 121590 (2023).

[8] Frias, J. P. & Nash, R. Microplastics: Finding a consensus on the definition. *Marine pollution bulletin* **138**, 145–147 (2019).

[9] Wang, S., Al-Hasni, N. S., Liu, Z. & Liu, A. Multifaceted aquatic environmental differences between nanoplastics and microplastics: behavior and fate. *Environment & Health* **2**, 688–701 (2024).

[10] Yin, K. *et al.* A comparative review of microplastics and nanoplastics: Toxicity hazards on digestive, reproductive and nervous system. *Science of the total environment* **774**, 145758 (2021).

[11] Series, A. P. C. Detection of various microplastics in human stool. *Ann Intern Med* **171**, 453–457 (2019).

[12] Leslie, H. A. *et al.* Discovery and quantification of plastic particle pollution in human blood. *Environment international* **163**, 107199 (2022).

[13] Nihart, A. J. *et al.* Bioaccumulation of microplastics in decedent human brains. *Nature medicine* **31**, 1114–1119 (2025).

[14] Enyoh, C. E., Duru, C. E., Ovuoraye, P. E. & Wang, Q. Evaluation of nanoplastics toxicity to the human placenta in systems. *Journal of Hazardous Materials* **446**, 130600 (2023).

[15] Lu, L., Wan, Z., Luo, T., Fu, Z. & Jin, Y. Polystyrene microplastics induce gut microbiota dysbiosis and hepatic lipid metabolism disorder in mice. *Science of the total environment* **631**, 449–458 (2018).

[16] Mattsson, K. *et al.* Brain damage and behavioural disorders in fish induced by plastic nanoparticles delivered through the food chain. *Scientific reports* **7**, 11452 (2017).

[17] Marfella, R. *et al.* Microplastics and nanoplastics in atheromas and cardiovascular events. *New England Journal of Medicine* **390**, 900–910 (2024).

[18] Meides, N. *et al.* Quantifying the fragmentation of polypropylene upon exposure to accelerated weathering. *Microplastics and Nanoplastics* **2**, 23 (2022).

[19] Luo, Y. *et al.* Microplastic and nanoplastic debris left behind by a plastic water tank subjected to a mimicked bushfire. *Engineering Reports* **6**, e12875 (2024).

[20] Luo, Y., Naidu, R., Zhang, X. & Fang, C. Microplastics and nanoplastics released from a ppe mask under a simulated bushfire condition. *Journal of Hazardous Materials* **439**, 129621 (2022).

[21] Ghosh, S. *et al.* Mechanism of microplastic and nanoplastic emission from tire wear. *Soft Matter* **21**, 2782–2786 (2025).

[22] Monira, S., Roychand, R., Hai, F. I., Bhuiyan, M. & Pramanik, B. K. Microplastic fragmentation into nanoplastics by water shear forces during wastewater treatment: Mechanical insights and theoretical analysis. *Environmental Pollution* **364**, 125310 (2025).

[23] Suzuki, G. *et al.* Mechanical recycling of plastic waste as a point source of microplastic pollution. *Environmental Pollution* **303**, 119114 (2022).

[24] Menzel, T. *et al.* Degradation of low-density polyethylene to nanoplastic particles by accelerated weathering. *Science of The Total Environment* **826**, 154035 (2022).

[25] Suzuki, G. *et al.* Global discharge of microplastics from mechanical recycling of plastic waste. *Environmental Pollution* **348**, 123855 (2024).

[26] Singh, S. *et al.* Microplastics in landfill leachate: occurrence, health concerns, and removal strategies. *Journal of environmental management* **342**, 118220 (2023).

[27] Yang, Z. *et al.* Is incineration the terminator of plastics and microplastics? *Journal of Hazardous Materials* **401**, 123429 (2021).

[28] Dulal, N. *et al.* Slip-additive migration, surface morphology, and performance on injection moulded high-density polyethylene closures. *Journal of colloid and interface science* **505**, 537–545 (2017).

[29] Coates, J. *et al.* Interpretation of infrared spectra, a practical approach. *Encyclopedia of analytical chemistry* **12**, 10815–10837 (2000).

[30] Das, S. *et al.* Varying the oxidative functionalization of polypropylene films under quiescent conditions. *Macromolecules* (2026).

[31] Hernández-Fernández, J., Cano, H. & Reyes, A. F. Valoration of the synthetic antioxidant tris-(diterbutyl-phenol)-phosphite (irgafos p-168) from industrial wastewater and application in polypropylene matrices to minimize its thermal degradation. *Molecules* **28**, 3163 (2023).

[32] Habibzadeh, F. Statistical data editing in scientific articles. *Journal of Korean medical science* **32**, 1072–1076 (2017).

[33] Bolland, J. L. Kinetic studies in the chemistry of rubber and related materials. i. the thermal oxidation of ethyl linoleate. *Proceedings of the Royal Society of London. Series A. Mathematical and Physical Sciences* **186**, 218–236 (1946).

[34] Bolland, J. L. & Gee, G. Kinetic studies in the chemistry of rubber and related materials. ii. the kinetics of oxidation of unconjugated olefins. *Transactions of the Faraday Society* **42**, 236–243 (1946).

[35] Mowery, D. M. *et al.* Radiation oxidation of polypropylene: A solid-state ^{13}c-nmr study using selective isotopic labeling. *Radiation Physics and Chemistry* **76**, 864–878 (2007).

[36] Gugumus, F. Re-examination of the thermal oxidation reactions of polymers3. various reactions in polyethylene and polypropylene. *Polymer degradation and stability* **77**, 147–155 (2002).

[37] Achimsky, L., Audouin, L. & Verdu, J. Kinetic study of the thermal oxidation of polypropylene. *Polymer degradation and stability* **57**, 231–240 (1997).

[38] Philippart, J.-L., Sinturel, C. & Gardette, J.-L. Influence of light intensity on the photooxidation of polypropylene. *Polymer Degradation and Stability* **58**, 261–268 (1997).

[39] Adams, J. Analysis of the nonvolatile oxidation products of polypropylene i. thermal oxidation. *Journal of Polymer Science Part A-1: Polymer Chemistry* **8**, 1077–1090 (1970).

[40] Iring, M. *et al.* Thermal oxidation of linear low density polyethylene. *Polymer degradation and stability* **14**, 319–332 (1986).

[41] Scheirs, J., Bigger, S. W. & Delatycki, O. Effect of thermal oxidation on the spherulitic morphology of high-density polyethylene. *Journal of Polymer Science Part B: Polymer Physics* **29**, 795–804 (1991).

[42] Bueche, F. Mechanical degradation of high polymers. *Journal of Applied Polymer Science* **4**, 101–106 (1960).

[43] François-Heude, A. *et al.* Real-time quantitative analysis of volatile products generated during solid-state polypropylene thermal oxidation. *Polymer testing* **32**, 907–917 (2013).

[44] Bernstein, R. *et al.* The origins of volatile oxidation products in the thermal degradation of polypropylene, identified by selective isotopic labeling. *Polymer Degradation and Stability* **92**, 2076–2094 (2007).

[45] Bernstein, R. *et al.* Radiation–oxidation mechanisms: volatile organic degradation products from polypropylene having selective c-13 labeling studied by gc/ms. *Polymer Degradation and Stability* **93**, 854–870 (2008).

[46] Vaillant, D., Lacoste, J. & Dauphin, G. The oxidation mechanism of polypropylene: contribution of ^{13}c-nmr spectroscopy. *Polymer degradation and stability* **45**, 355–360 (1994).

[47] Slouf, M. *et al.* Relations between morphology and micromechanical properties of alpha, beta and gamma phases of ipp. *Polymer Testing* **67**, 522–532 (2018).

[48] Lanyi, F. J., Wenzke, N., Kaschta, J. & Schubert, D. W. A method to reveal bulk and surface crystallinity of polypropylene by ftir spectroscopy-suitable for fibers and nonwovens. *Polymer Testing* **71**, 49–55 (2018).

[49] Lambert, A. Glass transition measurements on polystyrene by differential scanning calorimetry. *Polymer* **10**, 319–326 (1969).

[50] Abraham, M. J. *et al.* Gromacs: High performance molecular simulations through multi-level parallelism from laptops to supercomputers. *SoftwareX* **1**, 19–25 (2015).

[51] Jorgensen, W. L., Maxwell, D. S. & Tirado-Rives, J. Development and testing of the opls all-atom force field on conformational energetics and properties of organic liquids. *Journal of the american chemical society* **118**, 11225–11236 (1996).

[52] Owens, D. K. & Wendt, R. Estimation of the surface free energy of polymers. *Journal of applied polymer science* **13**, 1741–1747 (1969).

[53] Hariharan, A., Kumar, S. K. & Russell, T. P. Reversal of the isotopic effect in the surface behavior of binary polymer blends. *The Journal of Chemical Physics* **98**, 4163–4173 (1993).

[54] Keith, H. & Padden Jr, F. Spherulitic crystallization from the melt. i. fractionation and impurity segregation and their influence on crystalline morphology. *Journal of Applied Physics* **35**, 1270–1285 (1964).

[55] Monegro, R. H., Krishnamoorti, R. & Robertson, M. L. Functionalization and repurposing of polypropylene to a thermoset polyurethane. *ACS Macro Letters* **13**, 1442–1448 (2024).

[56] Cebe, P. *et al.* Heat of fusion of polymer crystals by fast scanning calorimetry. *Polymer* **126**, 240–247 (2017).

[57] Hess, B. P-lincs: A parallel linear constraint solver for molecular simulation. *Journal of chemical theory and computation* **4**, 116–122 (2008).

[58] Bussi, G., Donadio, D. & Parrinello, M. Canonical sampling through velocity rescaling. *The Journal of chemical physics* **126** (2007).

[59] Parrinello, M. & Rahman, A. Polymorphic transitions in single crystals: A new molecular dynamics method. *Journal of Applied Physics* **52**, 7182–7190 (1981).

[60] Nosé, S. A unified formulation of the constant temperature molecular dynamics methods. *The Journal of Chemical Physics* **81**, 511–519 (1984).

[61] Hoover, W. G. Canonical dynamics: Equilibrium phase-space distributions. *Physical Review A* **31**, 1695–1697 (1985).

[62] Essmann, U. *et al.* A smooth particle mesh ewald method. *The Journal of chemical physics* **103**, 8577–8593 (1995).

Supplementary Files

This is a list of supplementary files associated with this preprint. Click to download.

- SupplementalSectionMNPLpapernature.pdf